MATERIALS SCIENCE

Anisotropic Liesegang pattern for the nonlinear elastic biomineral-hydrogel complex

Woojin Choi[1]†, Milae Lee[1]†, Hyungseok Yong[1]†, Deokjae Heo[2], Taesuk Jun[1], Hanwook Ryu[2], Ji-Yeong Kim[3], Dingyun Cui[1], Du Yeol Ryu[1], Sang-Young Lee[1], Sung-Hwan Choi[3], Byeong-Su Kim[4], Jiyu Kim[1], Se Yong Jung[5], Sangmin Lee[2]*, Jinkee Hong[1]*

The Liesegang pattern is a beautiful natural anisotropic patterning phenomenon observed in rocks and sandstones. This study reveals that the Liesegang pattern can induce nonlinear elasticity. Here, a Liesegang-patterned complex with biomineral-hydrogel repetitive layers is prepared. This Liesegang-patterned complex is obtained only when the biomineralization is performed under the supersaturated conditions. The Liesegang-patterned complex features a nonlinear elastic response, whereas a complex with a single biomineral shell shows a linear behavior, thus demonstrating that the Liesegang pattern is essential in achieving nonlinear elasticity. The stiff biomineral layers have buffered the concentrated energy on behalf of soft hydrogels, thereby exposing the hydrogel components to reduced stress and, in turn, enabling them to perform the elasticity continuously. Moreover, the nonlinear elastic Liesegang-patterned complex exhibits excellent stress relaxation to the external loading, which is the biomechanical characteristic of cartilage. This stress relaxation allows the bundle of fiber-type Liesegang-patterned complex to endure greater deformation.

INTRODUCTION

The anisotropic structure determines intriguing behavioral properties of biological systems. For instance, the human bones exhibit the repetitive and anisotropic combination of soft collagen fibers and stiff hydroxyapatites (HAPs). Because collagen provides flexibility and resilience to the bone, while HAP contributes hardness and strength, the human bones feature superior mechanical properties, representatively, an elastic modulus of ~20 GPa (1, 2). The anisotropically distributing collagen fibers within the soft elastin matrix drive the flaw-insensitive fatigue resistance of bovine pericardium (3). The morphing of ice plant (*Delosperma nakurense*) capsules when adapting to a humid environment is assisted by an anisotropic structure composed of a nonswellable lignin cell wall and hygroscopic cellulose interior (4). To emulate these natural features, the diverse hydrogel (HD)–based anisotropic structures have been developed through the shear force, electric field, magnetic field, directional ice freezing, ion diffusion, and three-dimensional printing techniques (5–8). In particular, these anisotropic patterns have mechanically reinforced the HD itself (9–12). Furthermore, because the applied stress could be buffered by the incorporated strong components [for instance, glassy polymers (13, 14), nanoparticles (15), and graphene (16)], the anisotropic pattern of soft HD and strong components would considerably improve the physical features of the entire complex material. Accordingly, the technologies for anisotropic patterning of soft HD and strong components are promising for advanced biomimetic and bioinspired material systems.

The Liesegang pattern is a naturally self-organized anisotropic precipitation pattern in sedimentary rocks and sandstones (17, 18).

Scientists have found that this periodic pattern is formed when the diffusion reaction–based self-assembly of mineral precursors is conducted under a nonequilibrium (19, 20). Accordingly, recent works artificially generated Liesegang patterns using charged nanoparticles (21), liquid metal (22), Ag^+ precipitation (23), polyelectrolytes (24), and biopolymer (25). Although the Liesegang patterning protocols have been partially established, the specific advantages of the Liesegang pattern are rarely discussed. Most recently, the Liesegang pattern was developed as a fingerprint for improving the tactile sensing efficiency of ionic skin (26) and as a recorder of information about external mechanical changes (27). However, the mechanism of how the Liesegang pattern determines the mechanical properties was hardly revealed. In this study, we have found the unreported necessity of the Liesegang pattern in realizing a nonlinear elastic biomineral-HD complex material. Here, the nonlinear elasticity indicates the materials that do not exhibit the linear Hookean behavior when they are operating in the larger deformation strain (28, 29).

Human cells and tissues feature nonlinear elasticity, enabling them to maintain their integrity by stiffening in response to external deformation (1, 30). For instance, biological gels composed of proteins (e.g., actin, collagen, fibrin, vimentin, and neurofilaments) exhibited nonlinear elasticity (31). Therefore, nonlinear elastic materials have tremendous potential in broad biomedical applications, representatively, tissue engineering (32). Researches show that nonlinear elastic HD fibers feature excellent cellular affinity (33, 34). Furthermore, extracellular matrix–like nonlinear elastic HDs were shown to facilitate the spreading, proliferation, and osteogenic differentiation of mesenchymal stem cells (35, 36). Recently, the nonlinear elastic encapsulation layer of electrode arrays enabled the bioelectronics to be conformally attached to the human heart and brain cortex, thereby improving the bioelectronics operation quality (37). In tandems with several synthetic nonlinear elastic polymers [representatively, glycol-functionalized polyisocyanide semiflexible hydrogels (38)], studying strategies for preparing nonlinear elastic materials would be necessary in the biomedical fields.

In this study, we studied the biomineralization kinetics by tuning the ionic strength (*I*) to achieve the HAP-HD complex material featuring the anisotropic Liesegang pattern and nonlinear elasticity. Here,

[1]Department of Chemical and Biomolecular Engineering, College of Engineering, Yonsei University, Seoul 03722, Republic of Korea. [2]School of Mechanical Engineering, Chung-ang University, 84, Heukseok-ro, Dongjak-gu, Seoul 06974, Republic of Korea. [3]Department of Orthodontics, Institute of Craniofacial Deformity, Yonsei University College of Dentistry, Seoul 03722, Republic of Korea. [4]Department of Chemistry, Yonsei University, Seoul 03722, Republic of Korea. [5]Department of Pediatrics, Yonsei University College of Medicine, Seoul 03722, Republic of Korea.
*Corresponding author. Email: jinkee.hong@yonsei.ac.kr (J.H.); slee98@cau.ac.kr (S.L.)
†These authors contributed equally to this work.

the biomineralization indicates the HAP growing phenomenon using Ca^{2+}- and PO_4^{3-}-rich HAP precursors (*39–41*). The biomineralization performed below the critical I led to the single HAP shell–covered complex (HSC). This HSC presented the typical elastic response of an HD (*42, 43*). Conversely, the Liesegang-patterned complex (LPC) was accomplished when I was beyond the supersaturation point. This LPC exhibited cell- and tissue-like nonlinear elastic behavior (*30, 44*). The rheological studies and finite element analysis (FEA) revealed that the strong HAP structures exclusively endured the concentrated energy on behalf of soft HD layers. This reduced stress in the HD components enabled them to consistently perform stress dissipation and elasticity. The nonlinear elastic LPC showed excellent stress relaxation capacity, which is also observed as the biomechanical feature of cartilage. This study reports a fundamental comprehension of the Liesegang pattern and a straightforward technique for acquiring a complex material with broad potential biomedical applications.

RESULTS

Fabrication and investigation of LPC

Figure 1A shows the biomineralization-based Liesegang patterning process of the LPC. First, the double-network HD was synthesized using acrylamide and sodium alginate (*45*). In particular, the ionic cross-linker Ca^{2+} acted as an initial nucleation site (*39*). The acrylamide network mainly contributed as a control group with evident linear elasticity to study the Liesegang pattern–induced nonlinear elasticity of LPC. Meanwhile, it was reported that the acrylamide network would hardly influence biomineralization kinetics analogously with other inert substrates for Liesegang patterning, for instance, gelatin (*24*), chitosan (*46*), and polyvinyl alcohol–polyvinyl pyrrolidone HDs (*47*). Subsequently, the HD was repeatedly exposed to two separate HAP precursor solutions containing PO_4^{3-} and Ca^{2+} ions individually to trigger the ionic diffusion, nucleation, and precipitation. The entire faces of the LPC became opaque, indicating that the HAP shell had grown. According to C 1s x-ray photoelectron spectroscopy (XPS) spectra, the LPC showed 31% decreased C=O intensity than the HD, indicating that HAP was sufficiently grown (fig. S1). When the LPC was sliced into thirds, the Liesegang patterns of HAP (LP-HAPs) were observed occupying inside the HD. Moreover, the intermediate HD (inter-HD) between the HAP shell and LP-HAP and the interior core of the HD (HD core) were recognized. Thereby, the LPC exhibited an anisotropic pattern. The LPC was subjected to Raman spectroscopy, as shown in Fig. 1B. Notably, Raman signals of unit domains of the Liesegang pattern were acquired. The HAP shell region presented a strong peak at 960 cm^{-1} originating from PO_4^{3-} of HAP (*48*). Meanwhile, the regions of the inter-HD and HD core did not show any peaks within 900 to 990 cm^{-1}. The LP-HAP exhibited an intense Raman signal of HAP. This finding was visualized by
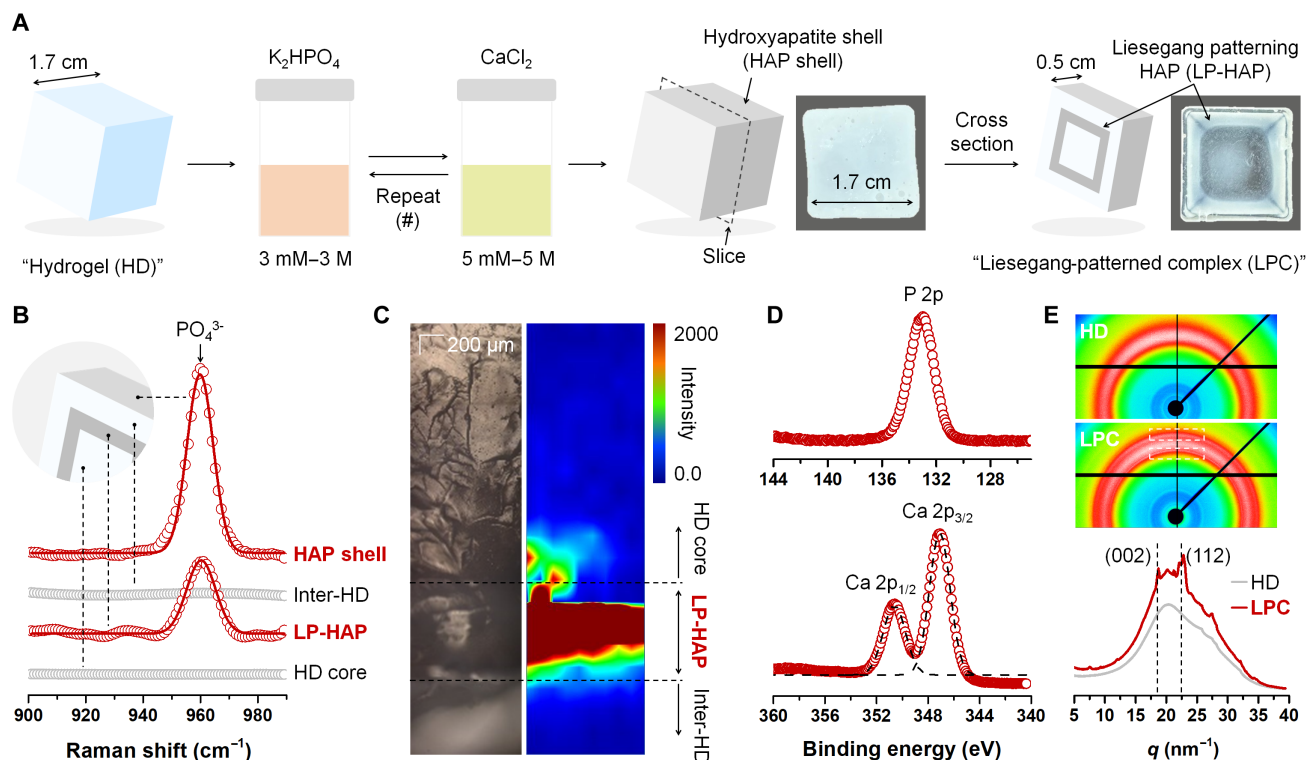
Fig. 1. Characterization of the LPC. (**A**) Fabrication process of LPC. A cubic HD is prepared with the volume of 4.91 cm^3. # is the exposure number of biomineral precursor. For example, # = 10 means that HD is immersed in PO_4^{3-} and Ca^{2+} for 10 times, respectively. LPC showed the same size as the HD. (**B**) Raman spectra within 900 to 990 cm^{-1} to study the unit sections of LPC: HAP shell, inter-HD, LP-HAP, and HD core. (**C**) Spatial distribution of HAP in LPC monitored through mosaic Raman mapping tool. Red indicates the strongest intensity of HAP-originated Raman signal at 960 cm^{-1}. (**D**) XPS of LPC. XPS spectra at 127 to 144 eV and 340 to 360 eV are related to P 2p and Ca 2p, respectively. (**E**) Two- and one-dimensional wide-angle x-ray scattering (WAXS) patterns of HD and LPC. Here, q is the scattering vector, where $q = (4\pi/\lambda) \sin(\theta/2)$. θ and λ are the scattering angle and wavelength of the incident x-ray beam, respectively.

tracking the HAP Raman signals using the mosaic Raman mapping within the area of the HD core–LP-HAP–inter-HD (Fig. 1C). These Raman experiments confirmed that the biomineralization selectively occurred at the LP-HAP and HAP shell regions, generating the distinct boundary within Liesegang patterns.

Deficient biomineralization results in the premature polymorph of HAP: amorphous calcium phosphate (ACP) (49). Because ACP is still metastable (50), the LPC should be composed of HAP to serve as the strong component within the anisotropic Liesegang pattern. Figure 1D shows the P 2p and Ca 2p XPS spectra of the LPC, involving the peaks at 133.1, 347.1, and 350.6 eV. Notably, the intense peak of Ca $2p_{3/2}$ is sensitively associated with the crystallinity in HAP (51). As shown in Fig. 1E, HD and LPC were subjected to wide-angle x-ray scattering (WAXS) experiments to comprehend their crystal structures. Only LPC presented obvious x-ray scattering patterns at 18.5 and 22.6 nm^{-1}. These two peaks are attributed to the (002) and (112) directions of thermodynamically stable HAP (51). Furthermore, when HD was exposed to the combination of Zn^{2+}-PO_4^{3-}, x-ray scattering signal was identical to HD, suggesting that the ionic diffusion and precipitation reaction should be accompanied (fig. S2) (20). Therefore, we determined that LPC featured the strong HAP–soft HD–strong HAP–soft HD anisotropic structure.

Mechanism of biomineralization-based anisotropic Liesegang patterning

As shown in Fig. 2A, biomineralization kinetics are substantially dependent on the I value of HAP precursor media (52). The ion permeation through the HD network is driven by a chemical potential gradient, leading to the positive relationship between ion penetration depth and I (the blue line in Fig. 2A) (53). In particular, the concentration difference (Δc) between the HD and surrounding medium determines the ion permeation flux density (J): $J = P(\Delta c/L)$, where L is the HD length and P indicates the permeability coefficient. Furthermore, the threshold energy for maturing the ionic clusters up to the nucleus size should be fulfilled for the nucleation and subsequent biomineralization (54). Hence, the biomineralization rates show the initial plateau, followed by an exponential increase during HAP growth and eventual saturation (the yellow lines in Fig. 2A). The rapid arrival at the saturation point could result in smaller HAPs (the green line in Fig. 2A) (55). In summary, when the value of I increases, the ion permeation becomes facilitated, the ions reach a deeper position, the biomineralization rate accelerates, and the size of HAP decreases (56).

Given that supersaturation means the distinctively increased I, the biomineralization behaviors would be unique under the supersaturated condition when compared to the normal HAP precursor media with low to moderate I (Fig. 2B) (20). When I is far below from supersaturation point, the slow ion flux leads to the shallow ion permeation depth, and HAP gradually grows from the ion-attaching nucleation surface and diffuses toward the core. Thereby, the entire trace of ion diffusion becomes a single and continuous HAP layer (Fig. 2C) (57, 58). When I was increased further, the ion permeation became intense, yielding a thicker HAP shell. This phenomenon is consistent with the reported single HAP shell formation scenario (39).

Notably, to yield a Liesegang pattern, an independent nucleation layer, separate from the continuous HAP shell growth in the outer layer, must be generated inside the HD. Considering the supersaturated condition, the nucleation could occur markedly at the deeper locations, which is essential to get out of the influence of continuous HAP shell formation and generate the LP-HAP (Fig. 2D) (59). At the same time, the supersaturated precursor accelerated the interfacial biomineralization into the HAP shell. Subsequently, these once-generated LP-HAP and HAP shell favorably drew the precursor ions. Because of this Ostwald ripening phenomenon, the intermediate ions were extracted to the regions of the LP-HAP or HAP shell, resulting in the distinct formation of the ion-depleted inter-HD area and the ion-rich Liesegang pattern.

Parameter studies of the Liesegang pattern formation mechanism

Three steps are essential for yielding LPC: pre-pH adjustment of HD, the biomineralization, and postincubation (Fig. 3A). The shrink during biomineralization step was an index of successful Liesegang patterning (fig. S3). Here, the parameters regulating each step were studied to understand the detailed mechanism of Liesegang patterning. First, the biomineralization step was controlled as shown in Fig. 3B: I was 0.033, 0.33, 3.3, and 33 M, and the exposure number to biomineral precursor (#) was 5 and 10. Previous works reported that the increasing # enabled the maturation of the HAP regardless of the short precursor exposure time (39, 57). Moreover, when $I = 33$ M, it indicates that the nonequilibrium supersaturated precursor was prepared. A thin HAP shell was formed under the $I = 0.033$ M and # = 5 condition. This HAP shell became relatively apparent when I was 0.33 M and # = 5. When I reached 3.3 M at # = 5, a distinct front boundary of the HAP shell was observed. The biomineralized complex with $I = 33$ M and # = 5 condition exhibited the inter-HD and LP-HAP. Although this Liesegang pattern was so far relatively ambiguous, $I = 33$ M led to an exclusive anisotropic structure unlike $I = 0.033$ to 3.3 M. These findings became evident when the biomineralization was conducted under # = 10. By increasing I until 3.3 M under # = 10 condition, the HAP shell continuously grew up to the biomineralization front boundary line observed in # = 5 case. The biomineralization under $I = 33$ M and # = 10 conditions resulted in the matured and apparent Liesegang pattern of the HAP shell–inter-HD–LP-HAP–HD core. In summary, the biomineralization using $I = 0.033$ to 3.3 M precursor results in HSC 1 to HSC 3 with different thicknesses of HAP shell, while the LPC was acquired selectively under $I = 33$ M condition.

The thickness of characteristic regions is shown in Fig. 3C. Regardless of # values, the HAP shell became thicker until $I = 3.3$ M. When # was increased from 5 to 10, HSC 1 ($I = 0.033$ M) and HSC 2 ($I = 0.33$ M) showed 255 and 183% increases in the HAP shell thickness, respectively. Meanwhile, the $I = 3.3$ M condition presented only a 112% increase, implying that the ionic permeation rate met the upper limit near $I = 3.3$ M. Considering the condition of $I = 33$ M and # = 5, the first appeared LP-HAP and inter-HD exhibited thickness values of 0.18 and 0.06 cm, respectively. After the Liesegang pattern formation, the HAP shell thickness was comparable to the case of $I = 0.33$ M. When # was 10, the LP-HAP became 133% thicker, while the thickness of the inter-HD was almost consistent, compared to the values when # = 5.

As shown in Fig. 3A, the standard condition of preparing LPC was determined as pH adjustment of HD to weak base; biomineralization under $I = 33$ M, # = 10, 1-min immersion conditions; and postincubation at 5 M Ca^{2+} medium. Subsequently, we varied the experiment conditions while fixing I and # to 33 M and 10 to comprehend the detailed mechanism of Liesegang patterning. As shown
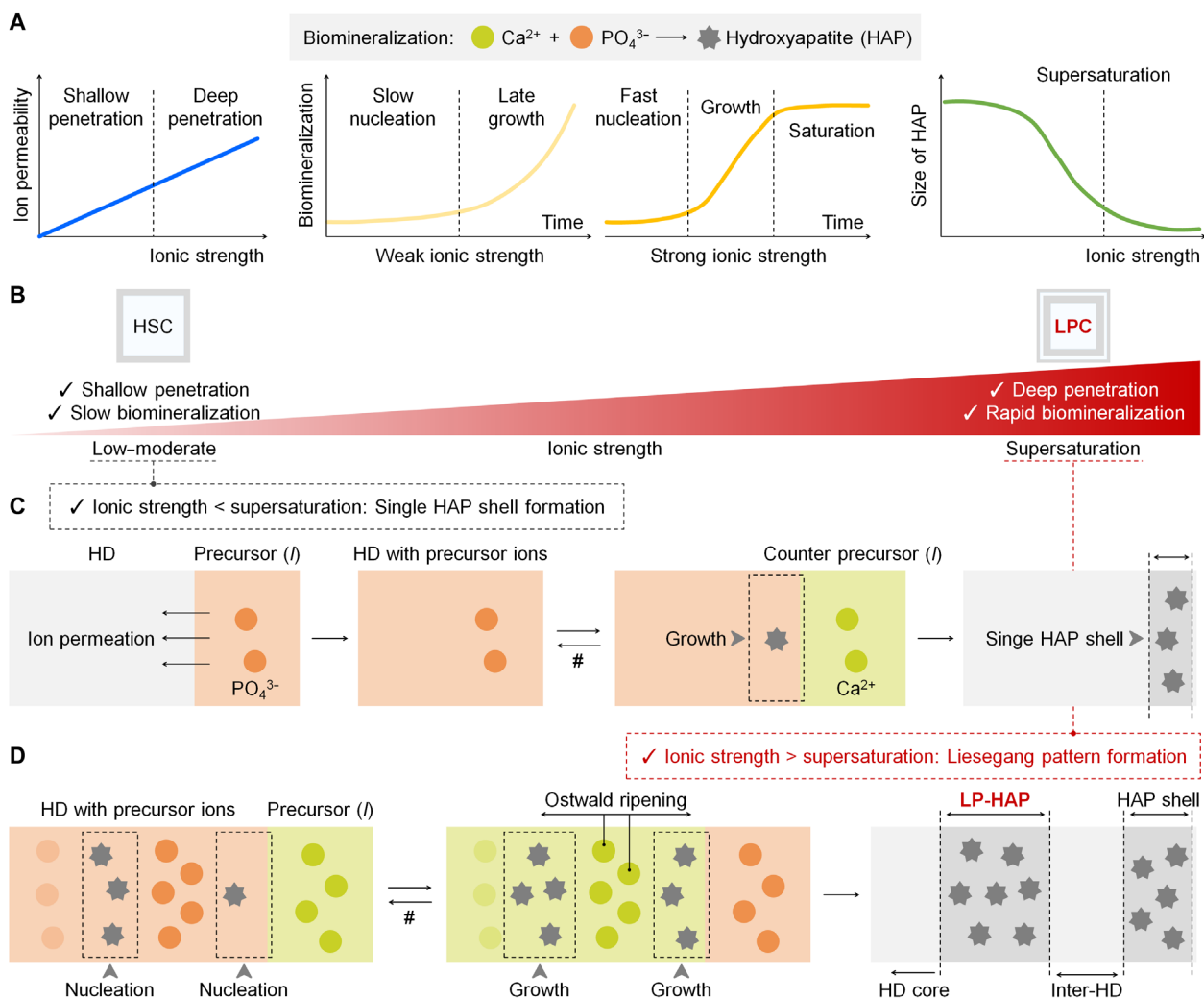
Fig. 2. Mechanism of biomineralization-based Lisegang patterning. (**A**) Influence of the ionic strength in the biomineralization kinetics. The ionic strength determines the position of HAP (blue line), the rate of HAP growth (yellow lines), and the size of HAP (green line). (**B**) The supersaturated precursor media enable deep penetration and rapid biomineralization to accomplish the Liesegang pattern and LPC. (**C** and **D**) Biomineralization scenarios during preparation (C) HSC with the nonsupersaturated media and (D) LPC at the supersaturation condition.

in Fig. 3D, the LP-HAP was not formed when the pH adjustment condition was changed from a weak base (pH 8.5) to a weak acid (pH 5.5). Given that acid disturbs the biomineralization and eventually demineralizes the HAP (60), the weak acid of HD prevented the initial nucleation inside HD necessary for LP-HAP growth. Through this experiment, we revealed that the initial nucleation notably influenced the eventual generation of the LP-HAP.

The value of I not only during the biomineralization step but also during the postincubation step was decisive in the Liesegang patterning. The gap between LP-HAP and HAP shell, i.e., inter-HD, was filled with the HAP when the postincubation was performed under 5 mM $CaCl_2$ (Fig. 3E). This result indicated that the weak ionic strength caused the shallow ion penetration and slow biomineralization from the HAP shell and thereby led to the interconnection between LP-HAP and HAP shell.

Furthermore, the once-generated LP-HAP and HAP shell were preferential nucleation sites where drawing the ions, facilitating the Ostwald ripening effect, and eventually closing the inter-HD

by their thickening. As suggested in Fig. 3F, the LP-HAP was still clear and slightly thicker when the immersion time during the biomineralization step was increased to 3 min. Meanwhile, when this immersion time reaches 5 min, the time for Ostwald ripening is prolonged, resulting in the almost merging of the HAP shell and LP-HAP. To additionally prove this finding, the once-made LPC was subjected to one more cycle of the entire LPC formation procedure. The diminishment of the inter-HD region was observed in this case as well (Fig. 3G). According to the parameter studies above, we conclude that the excess biomineralization should be prevented to yield a distinct Liesegang pattern, considering the Ostwald ripening effects that occurred from the boundaries of LP-HAP and HAP shell.

To capitalize on the sharpness of the Liesegang pattern, we engraved several holes in the HDs as the pathways for omnidirectional permeation, extraction, and precipitation of supersaturated ions. As shown in Fig. 3H, the squares with lengths of 0.5, 0.85, and 1.0 cm were patterned at 0.5-cm intervals. Then, the
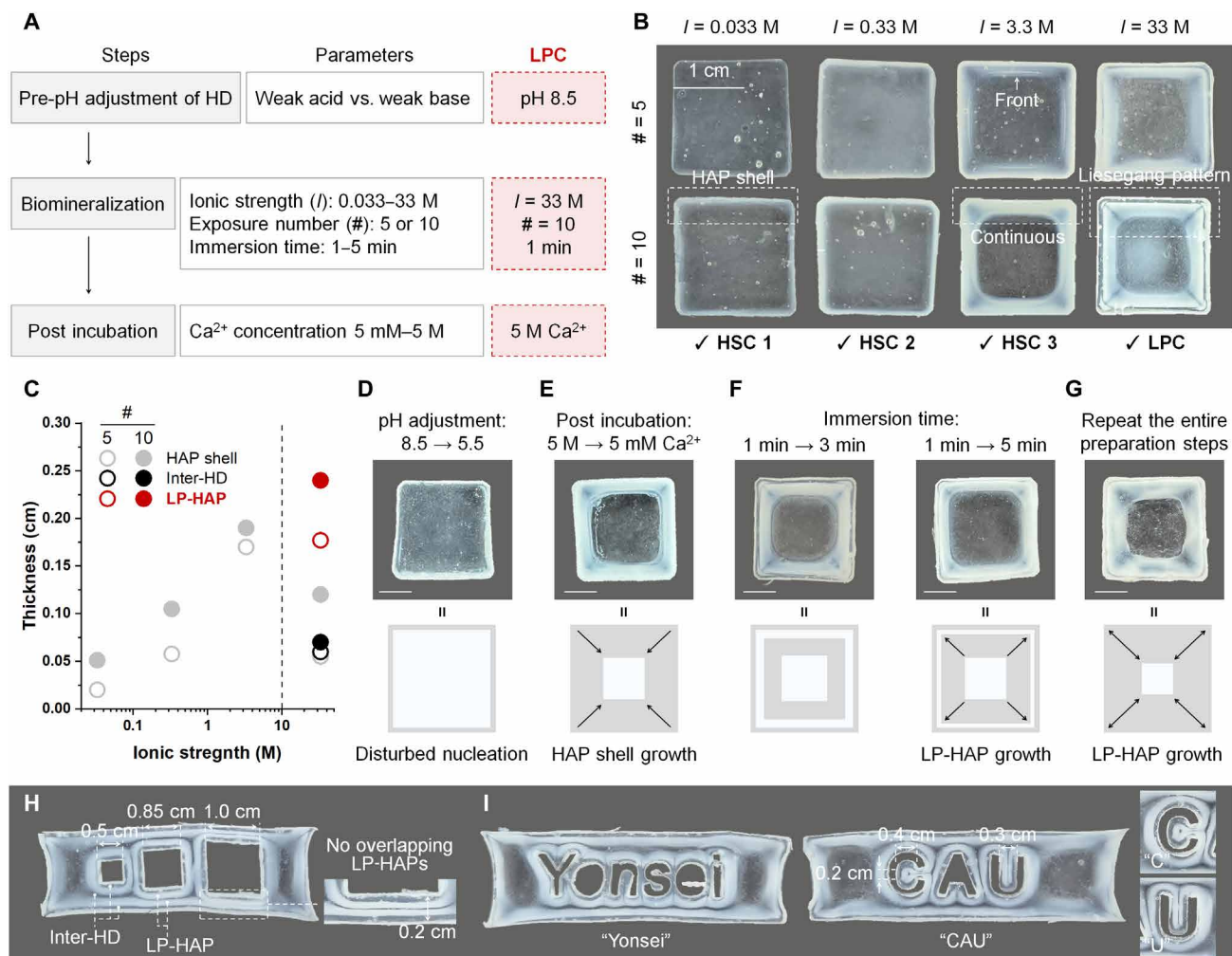
Fig. 3. Comprehension of parameters influential in Liesegang patterning. (**A**) Illustration of Liesegang patterning protocols and decisive parameters. (**B**) Images of biomineralized complexes prepared under different values of I (0.033 to 33 M) and # (5, 10). The size of all samples is identical to 2.89 cm². HSC 1 to HSC 3 mean the complexes biomineralized under I = 0.033 to 3.3 M and # = 10 conditions, while LPC corresponds to the sample biomineralized under I = 33 M and # = 10 conditions. (**C**) Thickness of specific regions (i.e., HAP shell, LP-HAP, and inter-HD) of HSC 1 to HSC 3, LPC biomineralized under the conditions of # = 5 (open symbols) and # = 10 (closed symbols). (**D** to **G**) Diverse LPCs obtained by differing experimental conditions, as denoted above in the images. Scale bars, 0.5 cm. (**H** and **I**) Fabrication of multiple Liesegang patterns with the (H) squares and (I) words. Because of the spec of the laser cutter, the shape of "e" was partially engraved.

biomineralization under I = 33 M and # = 10 condition was conducted. The multiple square-shaped Liesegang patterns were constructed within the single HD. The Liesegang patterns with circles, stars, and foot traces were also prepared (fig. S4). We observed that two LP-HAPs did not overlap despite being adjacent within 0.2 cm, implying the possibility of more complex Liesegang patterning. To clarify the assumption, Fig. 3I shows the Liesegang patterns with the words: "Yonsei and CAU (the authors' affiliation)." In particular, the characters "C" and "U" exhibited a limited Liesegang patterning area of less than 0.5 cm. Nevertheless, the neighboring LP-HAPs were not overlapped, and inter-HD regions were still monitored. We found that the proposed Liesegang patterning technology could exhibit an excellent resolution of ~0.2 cm when the biomineralization was conducted within the appropriate degree. That is, it can be expected that the Liesegang patterns can overlap when the immersion time exceeds 5 min.

Mechanical characterization of the LPC

Although the biomineralized complex with HAP shell–inter-HD–HAP core structure was reported, the correlation between the anisotropic structure and mechanical property was not revealed; meanwhile, the bioactivity of patterned HAPs was proved through the selective growth of the preosteoblast cells (61). Here, rheological studies were performed to comprehend the correlation between the anisotropic Liesegang pattern and the nonlinear elasticity. In particular, superposition rheology was used to monitor the storage modulus (G') within the broad deformation range, and G' represents the elastic behaviors. Regarding the general narrow deformation range, the G' profile difference between linear and nonlinear elastic materials is less obvious (the black line in Fig. 4A). Meanwhile, when the several G' profiles, which were accumulated as a function of time and temperature, were horizontally shifted on the basis of superposition theory, the master curves of linear and nonlinear elastic materials would exhibit a remarkable difference (the red line in Fig. 4A) (62).

In previous work, the extrapolated G' at a frequency of 10^8 rad s^{-1} was determined through superposition theory when the experiments were conducted within the frequency range of 0.1 to 100 rad s^{-1} (63). The elastic material presented a linearly increasing master curve. Conversely, the nonlinear elastic material showed a curved master curve with multiple plateaus. Time-temperature superposition is mainly used, whereas the time-kinetics (64) and time-humidity (65) models were additionally developed for specific purposes. Figure 4 (B to D) presents the fitted master curves of the HD, HSC 1 to HSC 3, and LPC by superpositing the G' profiles measured within 25° to 65°C at 5°C intervals under frequency sweeping. The horizontal shift factor (α_T) followed the Arrhenius equation–related activation energy (62, 66). Accordingly, as described in fig. S5, we measured the activation energy from the zero-frequency complex viscosity, thereby determining the α_T values of the HD, HSC 1 to HSC 3, and LPC.

As shown in Fig. 4B, the HD presented a linearly increasing G' profile within the slight G' increase (Δ) of 121%, confirming its outstanding linear elasticity (43). This linear elasticity was retained after the thin HAP shell was constructed in HSC 1 ($\Delta = 128\%$). When the HAP shell became thicker by increasing I to 0.33 M, HSC 2 showed an increased Δ of 154%. Furthermore, HSC 3 featured a more increased Δ of 240%, implying that the thicker HAP shell reinforced the entire complex material (Fig. 4C). Irrespective of the increasing values of Δ, HSC 1 to HSC 3 exhibited linear elasticity. The LPC presented a distinctive curved master curve compared to the HD

and HSC 1 to HSC 3, confirming its nonlinear elasticity (Fig. 4D). Under the low-frequency region, it showed a weaker Δ of 161%. After the critical frequency, G' increased in the nonlinear exponential growth with two plateaus. The LPC exhibited a substantial Δ of 483% within the nonlinear elastic regime. Moreover, the crossover point, where G' and loss modulus (G'') are being reversed, is the primary evidence of the nonlinear elasticity (67). HSC 3 did not show the crossover point, indicating that even a thick HAP shell could not surpass the elasticity of the background HD (fig. S6A). The LPC exhibited the crossover point in the lower frequency range (fig. S6B). Considering that the interface of HAP and HD is physically connected, this finding is comparable to the Maxwell-type nonlinear elastic behavior of a physically cross-linked poly(vinyl alcohol)-borax HD (68, 69).

We studied the loss factors of the HD, HSC 1 to HSC 3, and LPC to reveal how the anisotropic Liesegang pattern enabled the nonlinear elasticity (Fig. 4E). The loss factor indicates the energy dissipation efficiency, and a loss factor larger than 0.5 represents an excellent dissipation property (63). All samples exhibited a decreasing loss factor as the frequency increased. Regarding HSC 1 to HSC 3, only HSC 3 with the thickest HAP shell showed a loss factor larger than 0.5. However, this loss factor rapidly diminished below 0.5 when the frequency reached 10 Hz, proving that HSC 3 easily lost its energy dissipation property. The LPC presented a maximum loss factor of 2.62. Moreover, the loss factor of the LPC was larger than 0.5 until 10^3 Hz, suggesting that it was superior in energy dissipation.
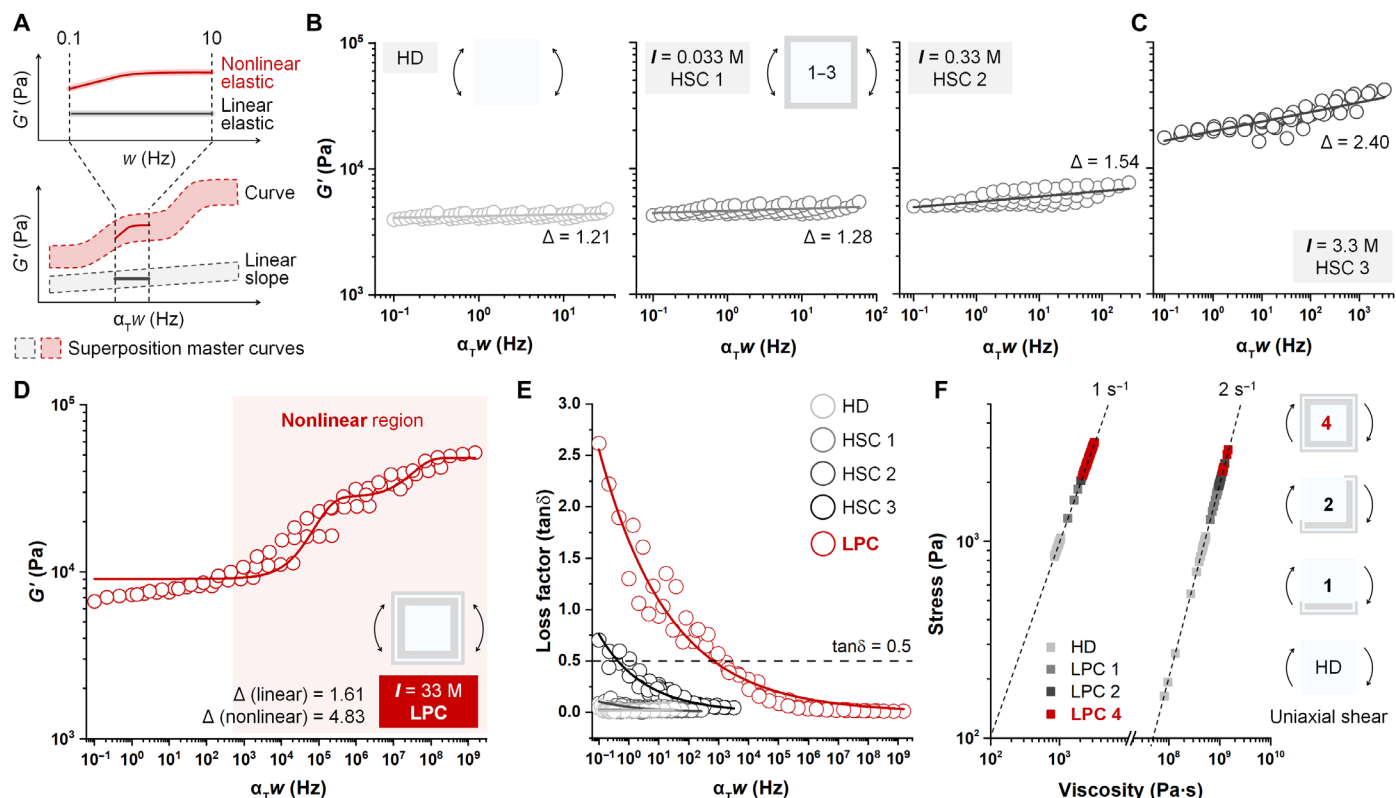
Fig. 4. Rheological investigation of the LPC. (**A**) Time-temperature superposition–based investigation of the frequency sweep rheological responses. G', α_T, and w mean the storage modulus, horizontal shift factor, and angular frequency (in hertz), respectively. (**B** to **D**) Superpositioned master curves of HD, HSC 1 to HSC 3, and LPC. The increases in G' were denoted as the symbol Δ. (**E**) Loss factors of HD, HSC 1 to HSC 3, and LPC. (**F**) Stress versus viscosity profiles of HD, HSC 1 to HSC 3, and LPC. The uniaxial shear is applied for 2 min.

Moreover, we prepared different LPCs (so-called LPC 1 and LPC 2) through partial biomineralization-based Liesegang patterning. As shown in Fig. 4F, LPC 1 denotes that only one side exhibited the Liesegang pattern, and LPC 2 indicates that the two adjacent vertical sides were subjected to biomineralization. The experimental section addresses their preparation protocols in detail. LPC 4 corresponds to the original LPC. The HD, LPC 1, LPC 2, and LPC 4 were studied under uniaxial shearing with different rates of 1 and 2 s^{-1} (fig. S7). When the shear rate was accelerated up to 2 s^{-1}, the HD exhibited a wide variation of stress and viscosity, meaning that its polymer network underwent considerable shear distortion. Regardless of the applied shear rate, the measured stresses were in the order of HD < LPC 1 < LPC 2 < LPC 4. In particular, the increasing number of Liesegang patterns resulted in a narrower stress versus viscosity plot. Hence, we revealed that the anisotropic Liesegang pattern was an essential structure in dissipating the applied loading and, consequently, in endowing the nonlinear elasticity to the LPC.

Subsequently, we performed FEA when the HD, HSC, and LPC were subjected to an identical compression force of 5 N or a torsion of 21.25 N·mm (Fig. 5A). As shown in Fig. 5 (B and C), the different equilibrium profiles after the deformation demonstrated that the stress distribution was considerably influenced by the Liesegang pattern. Regarding the HD under compression, its centroid exhibited more concentrated stress than the top and bottom surfaces (Fig. 5B, left). The stress smoothly increased along the azimuth angle and maximized up to 20.7 kPa at the boundary surface (70). This stress distribution profile was analogously observed in the HSC (Fig. 5B, middle). In particular, although the HAP shell accommodated more concentrated stress up to 26.0 kPa, the HD component of the HSC yielded an analogous stress distribution to the pure HD. Namely, the existence of the HAP shell rarely caused a positive influence on the stress distribution profile of the HSC. In contrast, the LPC presented a distinctive stress distribution profile in which most stress was biased toward the LP-HAP (Fig. 5B, right). The torsion experiments for the HD, HSC, and LPC resulted in stress distribution profiles identical to the compression tests (Fig. 5C).

In the compression test, the LP-HAP was exposed to maximally 148% more concentrated stress than the HD and HSC, considering the same distance from the centroid (Fig. 5D, top). Thereby, within the HD core of the LPC, 8.84 and 7.24% reduced stress developed
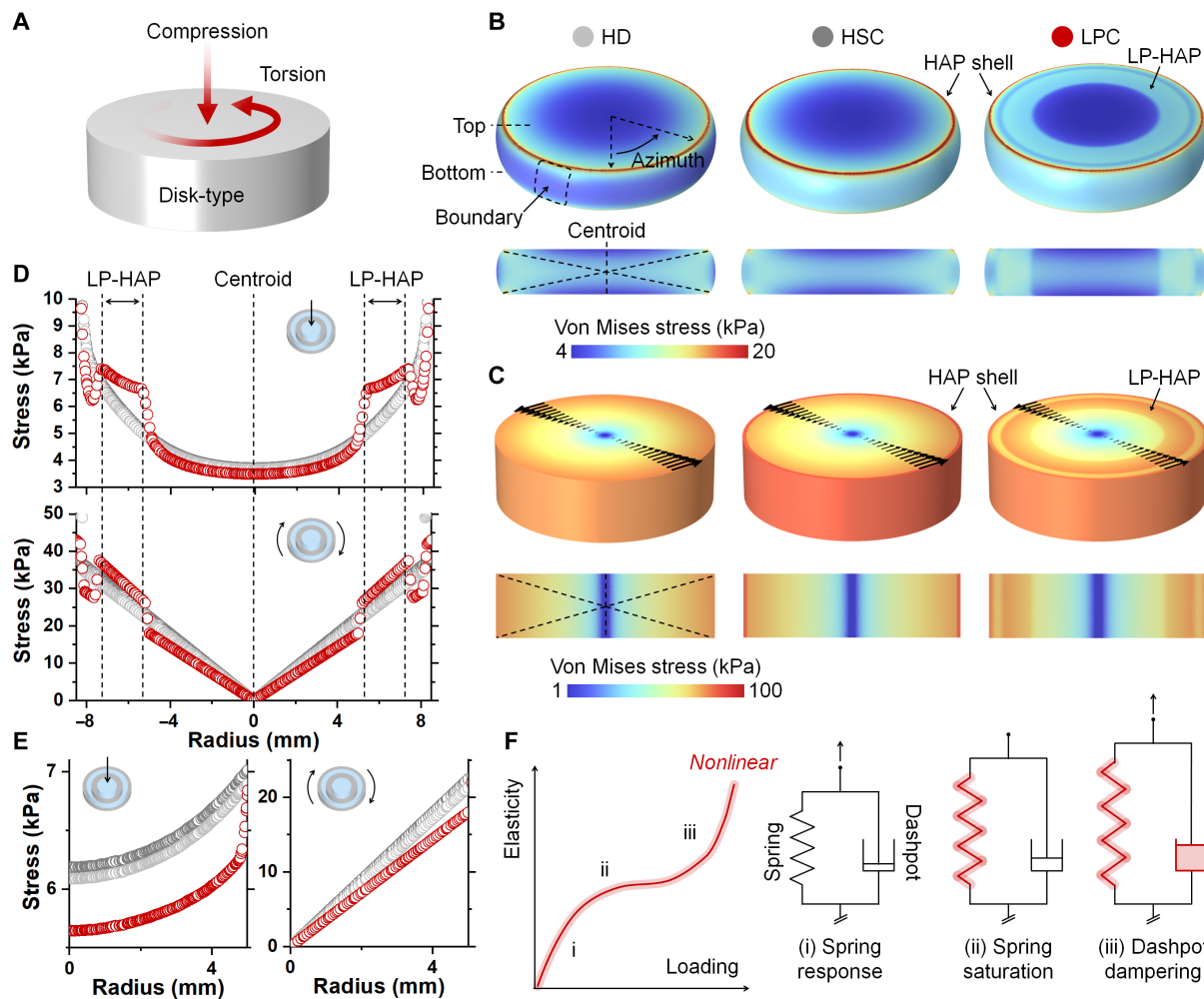

Fig. 5. FEA to study the influence of the Liesegang pattern. (**A**) Protocol of FEA. Here, the initial geometry of HD, HSC, and LPC was fixed to a cylinder. (**B** and **C**) Images of HD, HSC, and LPC when the equilibrium was reached after (B) compression and (C) torsion deformation. (**D**) Entire stress distribution of HD, HSC, and LPC. (**E**) Enlarged stress distribution near centroid. (**F**) Development of a spring-dashpot model of LPC to address how the nonlinear elasticity has been accomplished.

compared to the HD and HSC (Fig. 5E, left). Meanwhile, in the torsion test, given that the central part has less deformation, lower stress was observed in all cases. However, the distribution of stress that increases with distance shows a tendency similar to the compression test (Fig. 5D, bottom). In particular, near the boundary of the HD core in the torsion test, there was a 19.8% decrease in stress from the LPC (Fig. 5E, right).

These results indicated that the strong HAPs contributed as a stress concentrator in the LPC, considerably offsetting the energy within soft HD structures. This synergy accords with the spring-dashpot viscoelastic approximation in which the dashpot resists the loading and the spring component performs the elasticity (Fig. 5F) (71). When it comes to the LPC, the dashpot and spring correspond to the strong HAP and soft HD components, respectively. The remarkably diminished stress in the HD core and inter-HD was responsible for the nonlinear elasticity of the LPC. Despite the increasing loading on the LPC, the soft HD composites were exposed to minor stress because the strong HAP structures simultaneously buffered the concentrated energy without their failures. Thereby, the soft HD domains were capable of dissipating the stress and exerting their elasticity consistently.

Investigation of the LPC-based biomedical application

Here, we demonstrated the physical perspective potential of the LPC in the medical fields where nonlinear elasticity is essential for a satisfactory outcome. In particular, we studied whether the LPC could emulate the characteristic biomechanical behaviors of connective tissue cartilage. The cartilage consistently bears the compression and shear due to its superior stress-relaxing characteristic; thus, stress relaxation was regarded as one of the essential considerations in designing reliable artificial cartilage (72). Considering the excellent stress dissipation character of the LPC originating from its Liesegang pattern, we further studied its feasibility as an artificial finger cartilage for patients with osteoarthritis (Fig. 6A). At the current stage, the biological roles of cartilage, for instance, friction resistance (73), were not imparted to the LPC. The creep experiments were performed under a constant shear stress (0.1 kPa) and a hold time of 100 s. The HD showed an elastic creep response (fig. S8). Meanwhile, as shown in Fig. 6B, the LPC exhibited a viscoelastic deformation and recovery, which is also observed in collagen and alginate gels with excellent stress-relaxing features (74, 75).

Furthermore, we studied the stress relaxation profiles of the HD and LPC by applying a strain of 10 or 20% and holding for 1000 s (Fig. 6C). Prior works found that the relaxation profile during 1000 s notably affected cellular activities because the cells are generally sensitive to physical environment changes within 1 s (35, 76). Irrespective of the exerted strain, the HD maintained more than 95% of its stress as elastic energy during the first 100 s. In contrast, the LPC effectively relaxed the stress up to 75% over the same period. Moreover, only 70% of stress remained in the LPC at the end point. Figure 6D presents the cyclic compression experiments of the HD and LPC, and the hysteresis loop is correlated to the stress relaxation (77). The compression was applied up to the strain of 40%, considering the physiologically maximum strain of tissues, including the cartilage, which ranges from 30 to 40% (78, 79). Notably, the LPC demonstrated an apparent hysteresis loop compared to the HD. Furthermore, the LPC exhibited enhanced stress relaxation when the number of cycles increased (Fig. 6E). These validated that the LPC effectively relaxed shear and compression and

its promising potential as an artificial cartilage for dissipating the wear stress.

Subsequently, we prepared fiber-type HD (f-HD) and fiber-type LPC (f-LPC) with diameters of 2.90 mm and lengths of 5 to 10 cm. Figure 6F presents the images of the f-HD and f-LPC. HAP yields approximately zero transmittance, unlike the intrinsically transparent HD (80). Thus, the cross-sectional microscope image of the LPC presented a distinct boundary of the Liesegang pattern. In particular, the dark regions corresponded to the LP-HAP and the HAP shell, respectively. As shown in Fig. 6G, Raman spectroscopy studies of the f-LPC suggested that HAP was generated selectively in the regions of the LP-HAP and HAP shell. In terms of rheological investigation, f-LPC yielded a maximal 20-fold increase in G' compared to f-HD (fig. S9). Figure 6H shows the stress versus strain curves of the f-HD and f-LPC, where a uniform tensile force was applied at 5.0 mm min^{-1}. The f-HD showed an ultimate stress of 44.8 kPa and a fracture strain of 274.2%. Moreover, the f-LPC exhibited a highly reinforced ultimate stress of 74.7 kPa and a maximum strain of 358.6%. Hence, the f-LPC achieved an increased toughness of 15.2 kJ m^{-3}, whereas the f-HD showed a toughness of 8.83 kJ m^{-3}. These improvements in mechanical properties would be attributed to the stress relaxation capacity of f-LPC originating from its Liesegang pattern.

The mechanical behavior of a bundle of the f-LPCs was studied as shown in Fig. 6I. Here, a bundle with a length of 20 mm was composed of 19 f-HDs or f-LPCs. Under the external tensile loads of 1 and 2 N, the f-HD bundle showed mean stress of 13.2 and 32.1 kPa. Here, the mean stress indicates the average value of stress concentrated on the HD parts when tensile load is applied. As shown in fig. S10, the unit f-LPC within a bundle showed the Liesegang pattern–dependent stress-relaxing behavior, where the strong HD components buffered the stress, identical to the finding above. Hence, the f-LPC bundle presented a 18.2 and 20.2% reduced mean stress (10.8 and 25.6 kPa), respectively. Given the overall results, the LPC could be a potential candidate to replace the connective tissues that are subjected to repetitive loading.

DISCUSSION

Here, we demonstrated that the anisotropic Liesegang pattern was necessary for the nonlinear elastic complex material, LPC, and addressed the underlying mechanism. We prepared the LPC with the Liesegang pattern through supersaturation-assisted biomineralization. We figured out that I of the ionic precursor should be supersaturated to result in the Liesegang pattern. Meanwhile, I below the critical point led to the single biomineral shell. Furthermore, the degree of biomineralization should not be excessive to acquire the high-resolution Liesegang pattern. The mechanism of how the anisotropic Liesegang pattern caused the nonlinear elasticity was revealed through the rheological tests and FEA. The strong HAP shell and LP-HAP components buffered the concentrated energy, suppressing the failure of the soft HD matrix. Accordingly, the soft HD core and inter-HD were capable of exhibiting their elasticity consistently. Our model experiments found that this Liesegang pattern–based nonlinear elasticity enabled the LPC to potentially emulate the connective tissues. The LPC exhibited the stress-relaxing behaviors of the cartilage.

Despite the analogous physical behaviors with the cartilage, the LPC was partially limited in substituting the cartilage at the current
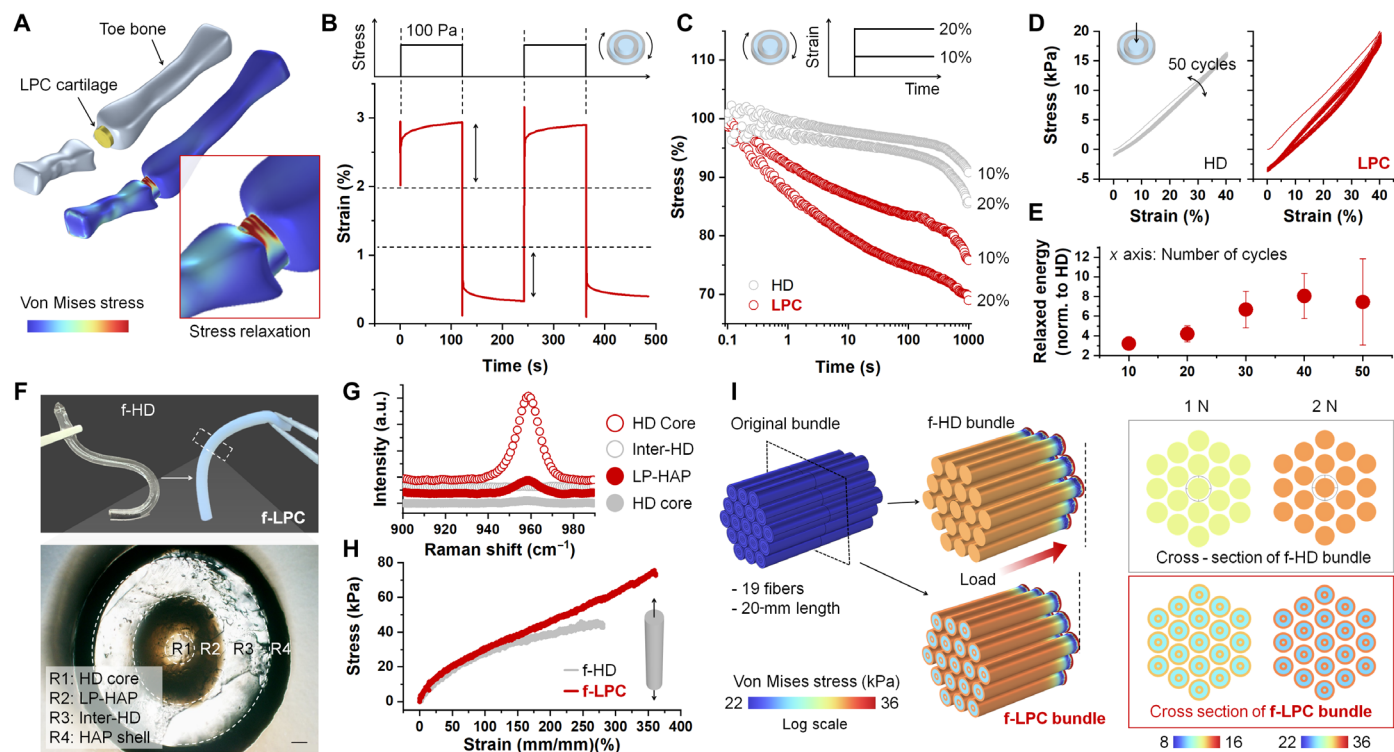
Fig. 6. Physical studies of the biomedical potentials using LPC. (**A**) FEA of the LPC-based artificial cartilage deployed at the metatarsal phalangeal joints. Here, we have assumed the case with a degenerative cartilage disease. (**B**) Shear creep test of the LPC. The double arrows indicate the viscoelastic response. (**C**) Stress relaxation profiles of the HD and LPC. The shear strains of 10 and 20% were applied. (**D**) Strain versus stress curves of the HD and LPC during 50-cycle compressions. The HD and LPC were compressed up to the strain of 40%. (**E**) Relaxed energy of LPC normalized to HD (means ± SD). (**F**) Photographs of f-HD and f-LPC. Below microscope image is the cross section of f-LPC. Scale bar, 200 μm. (**G**) Raman spectra of f-LPC within 900 to 990 cm^{-1}. The signal at 960 cm^{-1} indicates the HAP. a.u., arbitrary units. (**H**) Tensile stress versus strain curves of the f-HD and f-LPC. (**I**) FEA of the f-HD and f-LPC bundles. Each bundle comprises 19 f-HDs or f-LPCs with a length of 20 mm.

stage. In particular, the rapid biomineralization into the HAP might contribute to the simple Liesegang pattern with the four layers, which causes the upper limit of the mechanical properties of LPC. At the same time, we anticipate that the findings in this work could provide a clue to accomplishing cartilage-replacing material. The broad precipitation combinations could be used considering the supersaturation of the precursor solution has determined the anisotropic Liesegang patterning. That is, the elaborate design of the precipitation kinetics could lead to an advanced Liesegang pattern with multiple layers. Given that even a simple Liesegang pattern was capable of considerably affecting the entire mechanical properties of the LPC, a more complex Liesegang pattern might enable a strong and nonlinear elastic complex desirable in substituting the connective tissues.

MATERIALS AND METHODS
HD preparation
To prepare the HD precursor solution, 40% (w/v) of acrylamide (Sigma-Aldrich) and 2% (w/v) of sodium alginate (Sigma-Aldrich) were dissolved in distilled water. Then, 0.06% (w/v) of *N,N′*-methylenebisacrylamide (Sigma-Aldrich) was further added as a cross-linker. Next, 0.26% (w/v) of CaSO$_4$ (Sigma-Aldrich) was introduced, followed by 0.16% (w/v) of ammonium persulfate (Sigma-Aldrich) and 0.1% (v/v) of *N,N,N′,N′*-tetramethylethylenediamine (Sigma-Aldrich) to obtain the final precursor solution. This HD

precursor solution was poured into the poly(methyl methacrylate) and silicon molds, and then thermal polymerization was performed at 60°C for 1 hour. In detail, a poly(methyl methacrylate) cuvette was used to prepare the squared samples, and a silicon tube (inside diameter, 2 mm) was used for fiber-type samples. The obtained HDs were immersed in dichloromethane (Sigma-Aldrich) to loosen the molds and easily take the HDs out. The HDs were washed with distilled water for 1 day and stored in 40 mM tris buffer (pH 8.5) for 1 day.

Biomineralization
To obtain HSC 1, the HD was immersed in 3 mM K$_2$HPO$_4$ solution for 1 min and then washed with distilled water for 10 s. Subsequently, it was transferred to 5 mM CaCl$_2$ solution for 1 min and washed for 10 s. This biomineralization process was repeated for # times (here, # = 5 and 10). This sample was immersed in 5 mM CaCl$_2$ solution at 37°C for 1 day. This postincubation step was essential to mature the potentially residual ACP into HAP (*39, 57*). Last, the sample was transferred to distilled water at 4°C for sufficient swelling. The combination of 30 mM K$_2$HPO$_4$ and 50 M CaCl$_2$ and the same process as the HSC 1 preparation were used to prepare HSC 2. For HSC 3, 300 mM K$_2$HPO$_4$ solution and 500 mM CaCl$_2$ solution were used. To prepare the LPC, the HD was immersed in 3 M K$_2$HPO$_4$ solution and 5 M CaCl$_2$ solution following the experimental protocols above. The postincubation was performed in CaCl$_2$ solution with the same ionic strength as the biomineralization process. The HDs with the

average dimensions of 1.7 cm by 1.7 cm by 2.5 cm (width × length × height) are used for the experiments with unit 15 ml of precursor solution. A laser cutting machine (X252, GCC Co.) with a diameter of 1.0-cm laser (power, 4; speed, 0.1) was used to engrave various patterns in the HD. Then, the HDs were biomineralized into the LPC according to the process above. LPC 1 and LPC 2 were prepared by controlling the biomineralization location of the HD. To prepare LPC 1, only one side of the HD was immersed in the precursor solution. For LPC 2, the LPC formation procedure was performed using the LPC 1; in particular, the HD side adjacent to the patterned side of the LPC 1 was immersed in the precursor solution.

Characterization

LPC and f-LPC were analyzed by Raman spectroscopy (XploRA PLUS, HORIBA Scientific) with a 10× objective (numerical aperture = 0.25), a 532-nm laser, and a 1800 g mm^{-1} grating spectrometer. The laser was irradiated for 60 s and repeated five times. XPS (K-ALPHA, Thermo Fisher Scientific) was used to study the P 2p and Ca 2p spectra of the LPC and C 1s spectra of both the HD and LPC. WAXS experiments were performed using the 4C beamline at the Pohang Light Source.

Mechanical investigation

For time-temperature superposition, the shear moduli were measured under increasing temperature (25° to 60°C) using a rheometer (MCR 302, Anton Paar). A preload of 5.0 N, an angular frequency from 100 to 0.1 rad s^{-1}, and a constant shear strain of 1% were applied to the samples (thickness = 5.0 mm, N = 2 to 3). The viscosity versus shear stress profiles of LPC 1 to LPC 4 samples (thickness = 5.0 mm, N = 2 to 3, preload = 5.0 N) were obtained by presetting the shear rate as 1 and 2 s^{-1}. Creep recovery tests on the HD (thickness = 3.5 mm, N = 2 to 3, preload = 1.65 N) and LPC (thickness = 3.5 mm, N = 2 to 3, preload = 1.65 N) were performed with a constant shear stress of 100 Pa using a parallel plate geometry (25 mm in diameter). For the stress relaxation investigation, the HD (thickness = 3.5 mm, N = 2 to 3, preload = 1.65 N) and LPC (thickness = 3.5 mm, N = 2 to 3, preload = 1.65 N) samples were measured at 10 and 20% constant strain. These creep and relaxation experiments were carried out at 37°C. The HD and LPC were subjected to cyclic compression tests using a laboratory-made jig. The jig was made of 90°-bended polyethylene terephthalate glycol–modified. These jigs clamped to the wedge grips of the universal testing machine (Model 3366, Instron) to stably support and compress the samples for the tests. Then, the cyclic compression tests were performed using the HD (N = 3) and LPC (N = 3) with the height of 7.5 mm. The compression and recovery speed was set to 50 mm min^{-1}. The fiber-type samples (N = 2 to 3) with 4 cm in length were subjected to the tensile test using the Instron universal testing machine mentioned above. The tensile strain versus stress curves were measured by applying the tension at a rate of 20 mm min^{-1} until the samples failed. Rheological test–based strain sweep experiments were also performed for the fiber-type samples (length = 3.4 mm, N = 2 to 3, preload = 1.65 N) with a constant angular frequency of 6.28 rad s^{-1}. No debris of HAP was generated during the mechanical studies of HSC 1 to HSC 3 and LPC.

Finite element modeling

The mechanical behavior based on the Liesegang patterns of the HD and HAP was implemented through FEA software (COMSOL Multiphysics). We reverse-calculated the modulus of the HAP region through tensile test results of the f-HD and f-LPC and the results of FEA. By adjusting the modulus of the HAP region, the reaction force curve of the simulation and experimental values was fitted, and through this, the modulus of the HAP region was calculated. Furthermore, to simulate the energy dissipation by the Liesegang patterns, the property curves, including the modulus, were interpolated at each interface (fig. S11). The mechanical properties used in all simulations are listed in table S1. In addition, the geometry and input conditions for each case are listed in tables S2 to S4.

Supplementary Materials

This PDF file includes:
Figs. S1 to S11
Tables S1 to S4

REFERENCES AND NOTES

1. C. F. Guimarães, L. Gasperini, A. P. Marques, R. L. Reis, The stiffness of living tissues and its implications for tissue engineering. *Nat. Rev. Mater.* **5**, 351–370 (2020).
2. A. K. Nair, A. Gautieri, S.-W. Chang, M. J. Buehler, Molecular mechanics of mineralized collagen fibrils in bone. *Nat. Commun.* **4**, 1724 (2013).
3. L. Zeng, F. Liu, Q. Yu, C. Jin, J. Yang, Z. Suo, J. Tang, Flaw-insensitive fatigue resistance of chemically fixed collagenous soft tissues. *Sci. Adv.* **9**, eade7375 (2023).
4. H. Quan, D. Kisailus, M. A. Meyers, Hydration-induced reversible deformation of biological materials. *Nat. Rev. Mater.* **6**, 264–283 (2021).
5. M. Hua, S. Wu, Y. Ma, Y. Zhao, Z. Chen, I. Frenkel, J. Strzalka, H. Zhou, X. Zhu, X. He, Strong tough hydrogels via the synergy of freeze-casting and salting out. *Nature* **590**, 594–599 (2021).
6. K. Sano, Y. Ishida, T. Aida, Synthesis of anisotropic hydrogels and their applications. *Angew. Chem. Int. Ed. Engl.* **57**, 2532–2543 (2018).
7. M. Tanaka, S. M. Montgomery, L. Yue, Y. Wei, Y. Song, T. Nomura, H. J. Qi, Turing pattern–based design and fabrication of inflatable shape-morphing structures. *Sci. Adv.* **9**, eade4381 (2023).
8. Q. L. Zhu, C. F. Dai, D. Wagner, O. Khoruzhenko, W. Hong, J. Breu, Q. Zheng, Z. L. Wu, Patterned electrode assisted one-step fabrication of biomimetic morphing hydrogels with sophisticated anisotropic structures. *Adv. Sci.* **8**, 2102353 (2021).
9. J. Kim, G. Zhang, M. Shi, Z. Suo, Fracture, fatigue, and friction of polymers in which entanglements greatly outnumber cross-links. *Science* **374**, 212–216 (2021).
10. G. Nian, J. Kim, X. Bao, Z. Suo, Making highly elastic and tough hydrogels from doughs. *Adv. Mater.* **34**, e2206577 (2022).
11. H. Yuk, T. Zhang, S. Lin, G. A. Parada, X. Zhao, Tough bonding of hydrogels to diverse non-porous surfaces. *Nat. Mater.* **15**, 190–196 (2016).
12. X. Li, K. Cui, Y. Zheng, Y. N. Ye, C. Yu, W. Yang, T. Nakajima, J. P. Gong, Role of hierarchy structure on the mechanical adaptation of self-healing hydrogels under cyclic stretching. *Sci. Adv.* **9**, eadj6856 (2023).
13. G. Zhang, J. Kim, S. Hassan, Z. Suo, Self-assembled nanocomposites of high water content and load-bearing capacity. *Proc. Natl. Acad. Sci. U.S.A.* **119**, e2203962119 (2022).
14. G. Zhang, T. Yin, G. Nian, Z. Suo, Fatigue-resistant polyurethane elastomer composites. *Extreme Mech. Lett.* **48**, 101434 (2021).
15. E. A. Appel, M. W. Tibbitt, M. J. Webber, B. A. Mattix, O. Veiseh, R. Langer, Self-assembled hydrogels utilizing polymer–nanoparticle interactions. *Nat. Commun.* **6**, 6295 (2015).
16. X. Yu, H. Cheng, M. Zhang, Y. Zhao, L. Qu, G. Shi, Graphene-based smart materials. *Nat. Rev. Mater.* **2**, 17046 (2017).
17. K. H. Stern, The Liesegang phenomenon. *Chem. Rev.* **54**, 79–99 (1954).
18. E. Nakouzi, O. Steinbock, Self-organization in precipitation reactions far from the equilibrium. *Sci. Adv.* **2**, e1601144 (2016).
19. H. Nabika, M. Itatani, I. Lagzi, Pattern formation in precipitation reactions: The Liesegang phenomenon. *Langmuir* **36**, 481–497 (2020).
20. A. Arango-Restrepo, D. Barragán, J. M. Rubi, Nonequilibrium self-assembly induced Liesegang rings in a non-isothermal system. *Phys. Chem. Chem. Phys.* **20**, 4699–4707 (2018).
21. I. Lagzi, B. Kowalczyk, B. A. Grzybowski, Liesegang rings engineered from charged nanoparticles. *J. Am. Chem. Soc.* **132**, 58–60 (2010).
22. Z. Xing, Z. Zhang, J. Ye, Z. Zhou, J. Gao, B. du, K. Yue, Q. Wang, J. Liu, Liesegang phenomenon of liquid metals on Au film. *Adv. Mater.* **35**, e2209392 (2023).
23. H. Nabika, M. Sato, K. Unoura, Liesegang patterns engineered by a chemical reaction assisted by complex formation. *Langmuir* **30**, 5047–5051 (2014).
24. Y. S. Cho, M. Moon, G. Hollo, I. Lagzi, S. H. Yang, Bioinspired control of calcium phosphate Liesegang patterns using anionic polyelectrolytes. *Langmuir* **38**, 2515–2524 (2022).

25. T. S. Babicheva, A. A. Konduktorova, S. L. Shmakov, A. B. Shipovskaya, Formation of Liesegang structures under the conditions of the spatiotemporal reaction of polymer-analogous transformation (salt→ base) of chitosan. *J. Phys. Chem. B* **124**, 9255–9266 (2020).

26. H. Qiao, S. Sun, P. Wu, Non-equilibrium-growing aesthetic ionic skin for fingertip-like strain-undisturbed tactile sensation and texture recognition. *Adv. Mater.* **35**, e2300593 (2023).

27. M. Morsali, M. T. A. Khan, R. Ashirov, G. Holló, H. T. Baytekin, I. Lagzi, B. Baytekin, Mechanical control of periodic precipitation in stretchable gels to retrieve information on elastic deformation and for the complex patterning of matter. *Adv. Mater.* **32**, 1905779 (2020).

28. L. A. Mihai, A. Goriely, How to characterize a nonlinear elastic material? A review on nonlinear constitutive parameters in isotropic finite elasticity. *Proc. Math. Phys. Eng. Sci.* **473**, 20170607 (2017).

29. M. Dennison, M. Jaspers, P. H. J. Kouwer, C. Storm, A. E. Rowan, F. C. MacKintosh, Critical behaviour in the nonlinear elastic response of hydrogels. *Soft Matter* **12**, 6995–7004 (2016).

30. F. Burla, Y. Mulla, B. E. Vos, A. Aufderhorst-Roberts, G. H. Koenderink, From mechanical resilience to active material properties in biopolymer networks. *Nat. Rev. Phys.* **1**, 249–263 (2019).

31. C. Storm, J. J. Pastore, F. C. MacKintosh, T. C. Lubensky, P. A. Janmey, Nonlinear elasticity in biological gels. *Nature* **435**, 191–194 (2005).

32. N. Khuu, S. Kheiri, E. Kumacheva, Structurally anisotropic hydrogels for tissue engineering. *Trends Chem.* **3**, 1002–1026 (2021).

33. M. Wang, S. Sun, G. Dong, F. Long, J. T. Butcher, Soft, strong, tough, and durable protein-based fiber hydrogels. *Proc. Natl. Acad. Sci. U.S.A.* **120**, e2213030120 (2023).

34. M. D. Davidson, M. E. Prendergast, E. Ban, K. L. Xu, G. Mickel, P. Mensah, A. Dhand, P. A. Janmey, V. B. Shenoy, J. A. Burdick, Programmable and contractile materials through cell encapsulation in fibrous hydrogel assemblies. *Sci. Adv.* **7**, eabi8157 (2021).

35. O. Chaudhuri, L. Gu, D. Klumpers, M. Darnell, S. A. Bencherif, J. C. Weaver, N. Huebsch, H. P. Lee, E. Lippens, G. N. Duda, D. J. Mooney, Hydrogels with tunable stress relaxation regulate stem cell fate and activity. *Nat. Mater.* **15**, 326–334 (2016).

36. O. Chaudhuri, L. Gu, M. Darnell, D. Klumpers, S. A. Bencherif, J. C. Weaver, N. Huebsch, D. J. Mooney, Substrate stress relaxation regulates cell spreading. *Nat. Commun.* **6**, 6365 (2015).

37. C. M. Tringides, N. Vachicouras, I. de Lázaro, H. Wang, A. Trouillet, B. R. Seo, A. Elosegui-Artola, F. Fallegger, Y. Shin, C. Casiraghi, K. Kostarelos, S. P. Lacour, D. J. Mooney, Viscoelastic surface electrode arrays to interface with viscoelastic tissues. *Nat. Nanotechnol.* **16**, 1019–1029 (2021).

38. P. H. J. Kouwer, M. Koepf, V. A. A. Le Sage, M. Jaspers, A. M. van Buul, Z. H. Eksteen-Akeroyd, T. Woltinge, E. Schwartz, H. J. Kitto, R. Hoogenboom, S. J. Picken, R. J. M. Nolte, E. Mendes, A. E. Rowan, Responsive biomimetic networks from polyisocyanopeptide hydrogels. *Nature* **493**, 651–655 (2013).

39. T. Nonoyama, S. Wada, R. Kiyama, N. Kitamura, M. T. I. Mredha, X. Zhang, T. Kurokawa, T. Nakajima, Y. Takagi, K. Yasuda, J. P. Gong, Double-network hydrogels strongly bondable to bones by spontaneous osteogenesis penetration. *Adv. Mater.* **28**, 6740–6745 (2016).

40. B. Wen, Y. Dai, X. Han, F. Huo, L. Xie, M. Yu, Y. Wang, N. An, Z. Li, W. Guo, Biomineralization-inspired mineralized hydrogel promotes the repair and regeneration of dentin/bone hard tissue. *NPJ Regen. Med.* **8**, 11 (2023).

41. K. Fukao, K. Tanaka, R. Kiyama, T. Nonoyama, J. P. Gong, Hydrogels toughened by biominerals providing energy-dissipative sacrificial bonds. *J. Mater. Chem. B* **8**, 5184–5188 (2020).

42. C. Yang, Z. Suo, Hydrogel ionotronics. *Nat. Rev. Mater.* **3**, 125–142 (2018).

43. M. Wang, P. Zhang, M. Shamsi, J. L. Thelen, W. Qian, V. K. Truong, J. Ma, J. Hu, M. D. Dickey, Tough and stretchable ionogels by in situ phase separation. *Nat. Mater.* **21**, 359–365 (2022).

44. O. Chaudhuri, J. Cooper-White, P. A. Janmey, D. J. Mooney, V. B. Shenoy, Effects of extracellular matrix viscoelasticity on cellular behaviour. *Nature* **584**, 535–546 (2020).

45. J.-Y. Sun, X. Zhao, W. R. K. Illeperuma, O. Chaudhuri, K. H. Oh, D. J. Mooney, J. J. Vlassak, Z. Suo, Highly stretchable and tough hydrogels. *Nature* **489**, 133–136 (2012).

46. B. Li, Y. Gao, X. Li, Y. Feng, Y. Zhou, Chitosan hydrogels with 3D Liesegang ring structure for rifampicin release. *J. Control. Release* **152**, e47–e49 (2011).

47. A. Sahu, B. B. Kanrar, D. Panda, Evolution of micron-spaced patterns within precipitating patterns of in situ synthesized silver nanoparticles in a nanodot-embedded PVA/PVP Film. *Langmuir* **37**, 4460–4467 (2021).

48. G. Montes-Hernandez, F. Renard, Nucleation of brushite and hydroxyapatite from amorphous calcium phosphate phases revealed by dynamic in situ Raman spectroscopy. *J. Phys. Chem. C* **124**, 15302–15311 (2020).

49. J. J. De Yoreo, P. U. P. A. Gilbert, N. A. J. M. Sommerdijk, R. L. Penn, S. Whitelam, D. Joester, H. Zhang, J. D. Rimer, A. Navrotsky, J. F. Banfield, A. F. Wallace, F. M. Michel, F. C. Meldrum, H. Cölfen, P. M. Dove, Crystallization by particle attachment in synthetic, biogenic, and geologic environments. *Science* **349**, aaa6760 (2015).

50. M. Schweikle, S. H. Bjørnøy, A. T. J. van Helvoort, H. J. Haugen, P. Sikorski, H. Tiainen, Stabilisation of amorphous calcium phosphate in polyethylene glycol hydrogels. *Acta Biomater.* **90**, 132–145 (2019).

51. A. Procopio, E. Malucelli, A. Pacureanu, C. Cappadone, G. Farruggia, A. Sargenti, S. Castiglioni, D. Altamura, A. Sorrentino, C. Giannini, E. Pereiro, P. Cloetens, J. A. M. Maier, S. Iotti, Chemical fingerprint of Zn–hydroxyapatite in the early stages of osteogenic differentiation. *ACS Cent. Sci.* **5**, 1449–1460 (2019).

52. S. Yao, B. Jin, Z. Liu, C. Shao, R. Zhao, X. Wang, R. Tang, Biomineralization: From material tactics to biological strategy. *Adv. Mater.* **29**, 1605903 (2017).

53. D. R. Paul, The solution-diffusion model for swollen membranes. *Sep. Purif. Methods* **5**, 33–50 (1976).

54. J. Nývlt, Kinetics of nucleation in solutions. *J. Cryst. Growth* **3-4**, 377–383 (1968).

55. G. M. Pound, V. K. L. Mer, Kinetics of crystalline nucleus formation in supercooled liquid Tin[1,2]. *J. Am. Chem. Soc.* **74**, 2323–2332 (1952).

56. P. U. P. A. Gilbert, K. D. Bergmann, N. Boekelheide, S. Tambutté, T. Mass, F. Marin, J. F. Adkins, J. Erez, B. Gilbert, V. Knutson, M. Cantine, J. O. Hernández, A. H. Knoll, Biomineralization: Integrating mechanism and evolutionary history. *Sci. Adv.* **8**, eabl9653 (2022).

57. W. Choi, U. Mangal, J.-Y. Park, J.-Y. Kim, T. Jun, J. W. Jung, M. Choi, S. Jung, M. Lee, J.-Y. Na, D. Y. Ryu, J. M. Kim, J.-S. Kwon, W.-G. Koh, S. Lee, P. T. J. Hwang, K.-J. Lee, U.-W. Jung, J.-K. Cha, S.-H. Choi, J. Hong, Occlusive membranes for guided regeneration of inflamed tissue defects. *Nat. Commun.* **14**, 7687 (2023).

58. K. Kahil, S. Weiner, L. Addadi, A. Gal, Ion pathways in biomineralization: Perspectives on uptake, transport, and deposition of calcium, carbonate, and phosphate. *J. Am. Chem. Soc.* **143**, 21100–21112 (2021).

59. M. Kanduč, W. K. Kim, R. Roa, J. Dzubiella, How the shape and chemistry of molecular penetrants control responsive hydrogel permeability. *ACS Nano* **15**, 614–624 (2021).

60. R. J. Lamont, H. Koo, G. Hajishengallis, The oral microbiota: Dynamic communities and host interactions. *Nat. Rev. Microbiol.* **16**, 745–759 (2018).

61. M. Wu, Y. Zhao, H. Jiang, X. Xu, D. Wang, X. Xu, Y. Zhou, H. Tan, C. Ding, J. Li, Self-organized spatiotemporal mineralization of hydrogel: A simulant of osteon. *Small* **18**, e2106649 (2022).

62. W. Choi, M. Choi, T. Jun, Y. Kim, D. Y. Ryu, N. K. Kim, H.-J. Lee, Y. Lee, S. H. Lee, W. Lee, M. Lee, K. Kang, J.-S. Kwon, J. G. Jang, H. Ha, J. Y. Choi, S. Lim, S. Lee, S. Y. Jung, J. Hong, Templated assembly of silk fibroin for a bio-feedstock-derived heart valve leaflet. *Adv. Funct. Mater.* **34**, 2307106 (2023).

63. J. Huang, Y. Xu, S. Qi, J. Zhou, W. Shi, T. Zhao, M. Liu, Ultrahigh energy-dissipation elastomers by precisely tailoring the relaxation of confined polymer fluids. *Nat. Commun.* **12**, 3610 (2021).

64. Z. Huang, X. Chen, S. J. K. O'Neill, G. Wu, D. J. Whitaker, J. Li, J. A. McCune, O. A. Scherman, Highly compressible glass-like supramolecular polymer networks. *Nat. Mater.* **21**, 103–109 (2022).

65. P. C. Suarez-Martinez, P. Batys, M. Sammalkorpi, J. L. Lutkenhaus, Time–temperature and time–water superposition principles applied to poly (allylamine)/poly (acrylic acid) complexes. *Macromolecules* **52**, 3066–3074 (2019).

66. P. R. Laity, C. Holland, Thermo-rheological behaviour of native silk feedstocks. *Eur. Polym. J.* **87**, 519–534 (2017).

67. A. Balogun, D. Lazarenko, F. Khabaz, R. Khare, Extending the timescale of molecular simulations by using time–temperature superposition: Rheology of ionic liquids. *Soft Matter* **17**, 7210–7220 (2021).

68. T. Narita, K. Mayumi, G. Ducouret, P. Hébraud, Viscoelastic properties of poly (vinyl alcohol) hydrogels having permanent and transient cross-links studied by microrheology, classical rheometry, and dynamic light scattering. *Macromolecules* **46**, 4174–4183 (2013).

69. L. Martinetti, O. Carey-De La Torre, K. S. Schweizer, R. H. Ewoldt, Inferring the nonlinear mechanisms of a reversible network. *Macromolecules* **51**, 8772–8789 (2018).

70. H. Zhao, S. Liu, Y. Wei, Y. Yue, M. Gao, Y. Li, X. Zeng, X. Deng, N. A. Kotov, L. Guo, L. Jiang, Multiscale engineered artificial tooth enamel. *Science* **375**, 551–556 (2022).

71. J. Luo, S. Li, J. Xu, M. Chai, L. Gao, C. Yang, X. Shi, Biomimetic strain-stiffening hydrogel with crimped structure. *Adv. Funct. Mater.* **31**, 2104139 (2021).

72. L. Fu, L. Li, Q. Bian, B. Xue, J. Jin, J. Li, Y. Cao, Q. Jiang, H. Li, Cartilage-like protein hydrogels engineered via entanglement. *Nature* **618**, 740–747 (2023).

73. J. Liu, S. Lin, X. Liu, Z. Qin, Y. Yang, J. Zang, X. Zhao, Fatigue-resistant adhesion of hydrogels. *Nat. Commun.* **11**, 1071 (2020).

74. S. Nam, K. H. Hu, M. J. Butte, O. Chaudhuri, Strain-enhanced stress relaxation impacts nonlinear elasticity in collagen gels. *Proc. Natl. Acad. Sci. U.S.A.* **113**, 5492–5497 (2016).

75. K. Adebowale, Z. Gong, J. C. Hou, K. M. Wisdom, D. Garbett, H. P. Lee, S. Nam, T. Meyer, D. J. Odde, V. B. Shenoy, O. Chaudhuri, Enhanced substrate stress relaxation promotes filopodia-mediated cell migration. *Nat. Mater.* **20**, 1290–1299 (2021).

76. V. Vogel, M. Sheetz, Local force and geometry sensing regulate cell functions. *Nat. Rev. Mol. Cell Biol.* **7**, 265–275 (2006).

77. L. Xu, C. Wang, Y. Cui, A. Li, Y. Qiao, D. Qiu, Conjoined-network rendered stiff and tough hydrogels from biogenic molecules. *Sci. Adv.* **5**, eaau3442 (2019).

78. H. Yuk, C. E. Varela, C. S. Nabzdyk, X. Mao, R. F. Padera, E. T. Roche, X. Zhao, Dry double-sided tape for adhesion of wet tissues and devices. *Nature* **575**, 169–174 (2019).

79. Y. Hua, H. Xia, L. Jia, J. Zhao, D. Zhao, X. Yan, Y. Zhang, S. Tang, G. Zhou, L. Zhu, Q. Lin, Ultrafast, tough, and adhesive hydrogel based on hybrid photocrosslinking for articular cartilage repair in water-filled arthroscopy. *Sci. Adv.* **7**, eabg0628 (2021).

80. M. Nakayama, S. Kajiyama, A. Kumamoto, T. Nishimura, Y. Ikuhara, M. Yamato, T. Kato, Stimuli-responsive hydroxyapatite liquid crystal with macroscopically controllable ordering and magneto-optical functions. *Nat. Commun.* **9**, 568 (2018).